

# Atom-by-Atom Synthesis of Multiatom-Supported Catalytic Clusters by Liquid-Phase Atomic Layer Deposition

Benjamin P. Le Monnier, Louisa Savereide, Murat Kılıç, Raphael Schnyder, Mounir D. Mensi, Claudia E. Avalos, Ursula Rothlisberger, and Jeremy S. Luterbacher\*



Cite This: *ACS Sustainable Chem. Eng.* 2022, 10, 3455–3465



Read Online

ACCESS |



Metrics & More



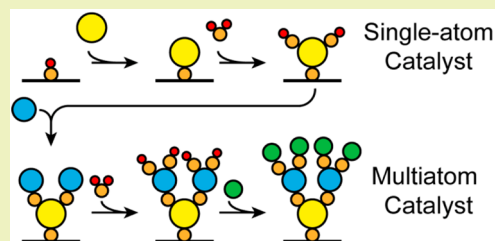
Article Recommendations



Supporting Information

**ABSTRACT:** Here, we introduce a method for the synthesis of atomically precise, supported, multiatom catalysts by liquid-phase atomic layer deposition. This technique is based on consecutive grafting reactions in mild conditions that build supported active sites atom by atom. The atomically controlled synthesis procedure led to the growth of well-defined multinuclear (Al, Mg, Si, Zn, and O) clusters. The composition of the clusters was verified by titrations ICP-OES, STEM-EDX, and XPS, while their structure was resolved from the synthesis sequence, elemental composition, and extensive characterization (X-ray absorption, solid-state NMR, STEM, XPS, and DFT calculations). Propane dehydrogenation was used as a probe reaction to demonstrate the potential to control and tailor the activity and stability of these catalytic clusters. Notably, we were able to alternatively multiply the initial activity of a known single-atom catalyst by 6 fold or improve its stability against thermal deactivation by simply using different elements and modifying the deposition sequence.

**KEYWORDS:** *Atomic layer deposition, Surface organometallic chemistry, Single-site catalyst, Rational catalyst design, Supported clusters*



## INTRODUCTION

Supported catalyst design has greatly evolved over the past decades thanks to improved understanding of relationships between the structure and activity of supported nanoparticles. However, commonly synthesized nanoparticle catalysts suffer from several intrinsic drawbacks, such as the inherently limited utilization of the supported metal, due to the atoms within the nanoparticle not participating in the catalytic process. Supported nanoparticles are also complicated systems to study and optimize due to the large number of coexisting heterogeneous active sites, which often leads to ambiguity over which is the true active site of the catalyst.<sup>1–3</sup> In contrast, interest in single-atom and single-site catalysts is steadily increasing.<sup>4,5</sup> This rise is due to the near complete atom utilization and the structural homogeneity. However, the limited tunability of such catalysts, which is inherent to the unique functionality of a single atom constrains the optimization of their catalytic features. Moreover, the low density of active sites caps the overall material productivity.<sup>6–8</sup> Surface organometallic chemistry methods have notably focused on making various single-site or single-atom catalysts, including with controlled structures and ligands.<sup>9,10</sup> Recently, supported multiatom catalysts (binuclear or dinuclear) are emerging as new alternatives for going beyond isolated atoms.<sup>11–13</sup> Examples of cooperative sites are well known in heterogeneous catalysis but are often difficult to isolate or synthesize in isolation (e.g., interfacial sites at the metal–support interface,<sup>14,15</sup> Ziegler–Natta catalysts<sup>16</sup>) and may feature a mix of different sites. Within these examples, some

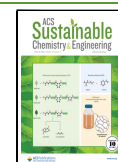
isolated systems have recently been observed,<sup>17,18</sup> but cases of rationally designed, supported, multiatom catalysts remain scarce.<sup>19–21</sup> Despite these promising catalytic results, this scarcity of examples can be explained by the lack of generic synthesis approaches for making defined multiatom systems, including in surface organometallic chemistry techniques which are often tailored to a specific site structure.<sup>9,10</sup> A simple reproducible method for atom-by-atom preparation of isolated multiatom sites would greatly facilitate the experimental assessment of the cooperativity and synergy between atoms, which is paramount to understanding surface reactivity.<sup>22</sup> Such a method would also provide a tool for the rational design of active sites.

In this work, we propose a general strategy based on atomic layer deposition (ALD) for the rational design of supported multiatom catalysts. ALD is generally a gas-phase technique that is designed for the deposition of thin films with atomic accuracy and is mostly used in the microelectronics field, although it is increasingly being explored for catalysis.<sup>23–25</sup> The principle is based on a four-step cycle (Figure 1a): (1) addition and adsorption of an excess of reagent A, (2) removal of unreacted A, (3) addition and adsorption of a counter-

**Received:** October 15, 2021

**Revised:** January 26, 2022

**Published:** March 10, 2022



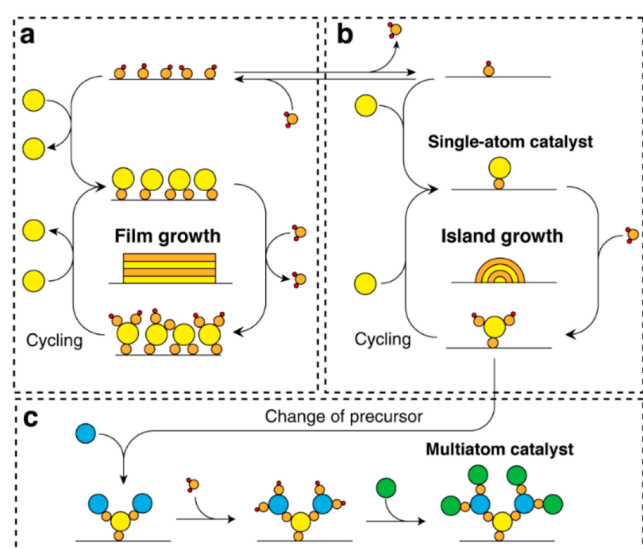


**Figure 1.** Representation of growth mechanisms and structures obtained using self-limited reactions in ALD. (a) Growth mechanism with a high number of adsorption sites or excess of precursors. Each layer fully covers the surface leading to the formation of a continuous film. (b) Growth mechanism with isolated adsorption sites and stoichiometric addition of reactants. The growth starts exclusively from isolated sites. The species grafted at the first layer can be used as single-atom catalysts, with subsequent growth from these sites leading to the formation of homogeneous clusters. (c) A variant of this mechanism where instead of cycling a precursor and a counter reactant different precursors are alternated.

reactant B, and (4) removal of unreacted B. The key features are the self-limited reactions between the reagents and the surface as well as the decoupling of each reaction into “half cycles”. At no point are both reactants present in the same phase, which avoids off-surface condensation. The thickness of the film is simply controlled by the number of cycles.

So far, ALD has been used in heterogeneous catalysis for the deposition of protective or active thin films,<sup>26–28</sup> nanoparticle growth,<sup>29–31</sup> single-atom catalysts<sup>32–34</sup> and, in only two examples we could find, for a dimeric site.<sup>35,36</sup> In microelectronics, the formation of nanoparticles was originally considered a defect of the procedure. The nucleation and growth of islands (or nanoparticles) is a known and usually unwanted phenomenon due to insufficient reactive sites on the surface (Figure 1b).<sup>37,38</sup> Such nucleation has been shown to be highly dependent on the functionality of the surface<sup>39,40</sup> and the nature of the deposited material.<sup>41,42</sup> In the gas phase, this phenomenon is difficult to induce or control when the substrate and deposited layer are highly compatible (good wettability), which almost invariably leads to the formation of a continuous film at the temperatures required to vaporize the precursors.<sup>37</sup> Small clusters that are not strongly bound to the substrate will gather by surface diffusion and form nanoparticles.<sup>43</sup> Finally, when using water in excess as the counter-reactant, rapid rehydroxylation of the surface can occur, which prevents controlled cluster growth.<sup>44</sup> For all these reasons, controlled island growth at low cycle numbers has been largely unexploited in gas-phase ALD.

In previous work, we developed a method for liquid-phase atomic layer deposition that substituted the injection of precisely measured stoichiometric quantities of precursors for purging cycles.<sup>45</sup> The use of stoichiometric quantities of

precursors avoided off-surface growth by limiting the excess of precursor use instead of relying on the evacuation of said precursor during the purge. This process led to coatings that were largely indistinguishable from conventional gas-phase ALD. Interestingly, when a dehydroxylated support was used, we also observed that, under these stoichiometrically limited and mild conditions, island growth could be promoted and maintained throughout the deposition. This phenomenon resulted from the selective growth occurring only on targeted anchoring sites. In this study, we promoted and exploited this selective nucleation phenomenon by carefully chosen surface pretreatment and mild deposition conditions. By using the early stage of island growth and by varying the nature of the reagents, we demonstrate the possibility of designing both the structure and composition of a multiatom catalyst (Figure 1c). As a proof of concept, we prepared a series of catalysts by liquid-phase atomic layer deposition with commercial precursors. Catalytic propane dehydrogenation was selected as a model reaction to probe and isolate the influence of the structure and composition of the active sites on their reactivity.

## RESULTS AND DISCUSSION

**Supported Clusters Preparation.** A series of catalysts were prepared using a single batch of high-surface area dehydroxylated amorphous silica (0.6 OH/nm<sup>2</sup>, Figure 2a). The surface functionalities are essentially pendent hydroxyl groups (reactive) and oxo bridges (which are unreactive in our conditions). The procedure is an adaptation of well-established gas-phase ALD chemistry, but instead of excess quantities, we use stoichiometric injections in liquid phase at room temperature, which avoids the need for purging reactants. The stoichiometry was determined by titrating the surface with either the metal precursor or counter-reactant and measuring the release of the corresponding ligand. The stoichiometric quantity corresponded to the quantity of added reactant at which the ligand ceased to be released due to the self-limiting nature of the surface reaction (Figure 2b). The slope before the equivalence point is a measure of the number of reactions with the surface per precursor. For instance, when each aluminum precursor reacts only once with the surface, one molecule of methane was released per precursor leading to a slope of 1 (Figure 2b).

Reports studying both atomic layer deposition and surface organometallic chemistry have described alkyl aluminums including TMA reacting with an oxo bridge by alkyl transfer, which lead to the formation of silicon–carbon bonds.<sup>46,47</sup> We do not observe this here (or at least not significantly) as we were able to close the methane balance at room temperature, which would not have been possible if grafting through an alkyl transfer had occurred due to the lack of reactivity of alkyl silane toward water.<sup>48</sup> This means that our system allowed deposition exclusively on the pendent hydroxyl groups. The milder reactivity of TMA observed here likely results from the complexation with the solvent that stabilizes the TMA. This is consistent with the fact that TMA is dimeric when pure or solubilized in alkanes while it is monomeric when complexed with ethers.<sup>45,49</sup> The solvent presence is a selective grafting of precursors on pendent hydroxyl groups.

As we confirmed here, the formation of either a continuous film or an island, in this liquid-phase method, is only dictated by the density of anchoring sites.<sup>37</sup> This behavior appears to be unique to this procedure. Notably, surface rehydroxylation between cycles is prevented by several of this method’s

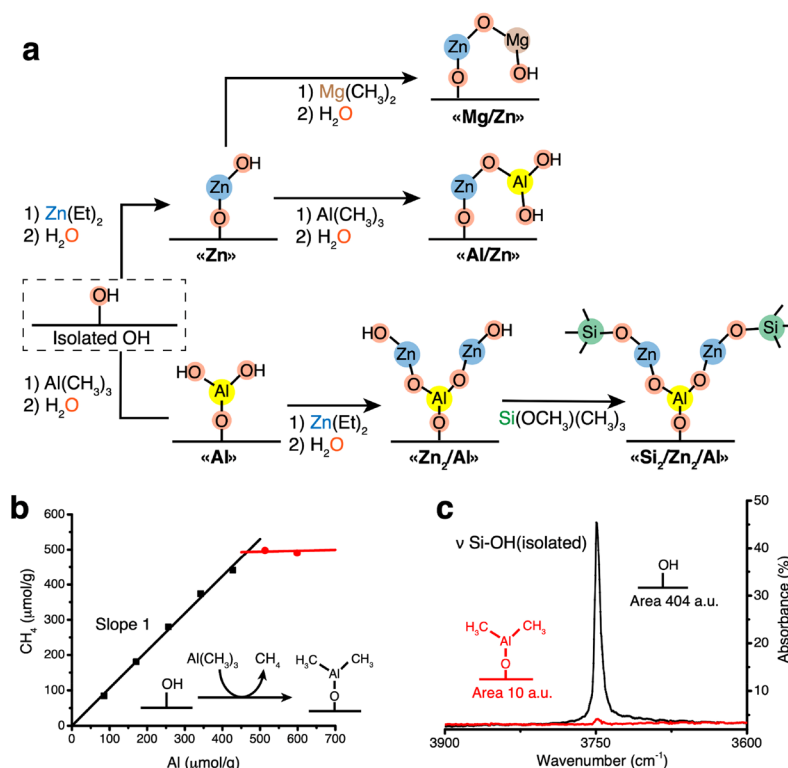


**Figure 2.** (a) Preparation steps of the various catalysts: starting with dehydroxylation of the silica surface followed by alternating precursor addition (trimethylaluminum, diethylzinc, or dimethylmagnesium) and the counter-reactant ( $\text{H}_2\text{O}$ ). The deposition of the first precursor creates single-atom catalysts. When more than one precursor is involved, we refer to it as a “multiatom catalyst”. The structures depicted represent the catalyst “as prepared” without showing any attached solvent. At high temperature, the pendent groups likely reform a bond with the surface by dehydroxylation. (b) Ligand release during the surface titration showing an increase of released methane when TMA is added to a dehydroxylated silica surface until all hydroxyl groups have been consumed, at which point the release ceases. (c) Diffuse reflectance infrared Fourier transform (DRIFTS) spectra showing isolated hydroxyl groups and their consumption after stoichiometric grafting of a precursor (the full spectra are available in Figure S1).

conditions, namely, the presence of an ether solvent, which solvates electrophilic atoms, the room-temperature reaction conditions, which slow surface hydroxylation, and the stoichiometric addition of water rather than an excess, which contributes to rehydroxylation, as is the case under typical gas-phase ALD conditions.<sup>44,49–51</sup> To ensure that isolated sites were present to begin with, an extensive dehydroxylation of the silica substrate was performed to prevent interaction between grafted species. After treatment at  $800\text{ }^\circ\text{C}$  under vacuum, the hydroxyl density measured by Grignard titration was  $0.55\text{ OH}/\text{nm}^2$ , which is equivalent to a statistical distance of  $7.5\text{ \AA}$  between sites and consistent with past work<sup>52</sup> and which was enough to consider the anchoring sites independent. The isolation of the remaining hydroxyl group was further confirmed by the titration slope (which was only 1) and was also observed by DRIFTS (Figure 2c). A sharp peak at  $3750\text{ cm}^{-1}$  was attributed to isolated hydroxyl groups,<sup>53</sup> and following the grafting of a stoichiometric layer of TMA, the signal completely disappeared (signals were normalized by the amorphous  $\text{SiO}_2$  vibrations), highlighting the full consumption of anchoring sites by the stoichiometric amount of precursor. The series of catalysts that was prepared included those prepared with only one precursor, trimethyl aluminum (TMA) and diethylzinc (DEZ), designated as Al and Zn catalysts, respectively, which we consider to be single-atom catalysts (Figure 2a). The structure and activity of these materials are already well described in the literature.<sup>3,54–56</sup> By depositing a

second layer on top of these initial isolated active sites, we prepared multiatom catalysts using combinations of TMA, DEZ, and dimethylmagnesium (DMM), which we designated as Al/Zn, Mg/Zn, and  $\text{Zn}_2/\text{Al}$  (Figure 2a). Finally, a third layer was deposited onto  $\text{Zn}_2/\text{Al}$  to form  $\text{Si}_2/\text{Zn}_2/\text{Al}$  using trimethylmethoxysilane.

Importantly, the quantity of metal that is deposited is entirely dictated by the available sites on the substrate, which are measured by surface titration (Experimental Section). The element ratio is in fact set by this site availability. In the example of catalyst  $\text{Zn}_2/\text{Al}$ , that has a Zn:Al ratio of about 2, an aluminum titration showed that the total quantity of aluminum deposited was  $459\text{ }\mu\text{mol}/\text{g}$  (Figure S2). The following titration of water indicates that  $889\text{ }\mu\text{mol}/\text{g}$  of water could react with the surface. Finally, the zinc titration showed that  $870\text{ }\mu\text{mol}/\text{g}$  of zinc could react with the surface. Consequently, the Zn:Al ratio was imposed by the material and equaled 1.9. Changing the sequence (the order of precursor addition) changed the surface composition and thus changed the titration results along with the resulting elemental ratio.

Surface reactions between each precursor (DEZ, TMA, and Grignard) and dried silica lead to a similar quantity of ligand released (all numbers are within 5%, Figure S2, although this spread may vary with supports and reagents). Considering that it takes one hydroxyl group to release one ligand (Figure 2b), the measured number of available hydroxyl groups is therefore similar in all cases. This indicates that all titrations are

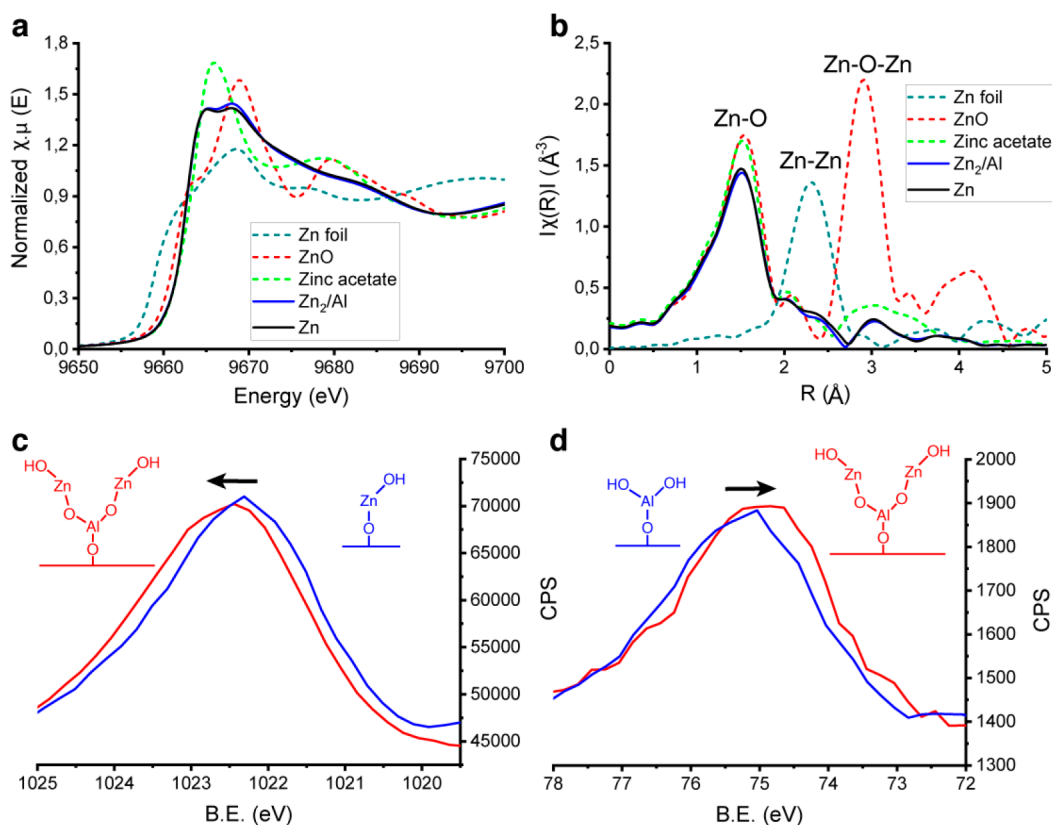


**Figure 3.** (a) XANES spectra of Zn foil, ZnO, and zinc acetate as references and the calcined Zn single-atom catalyst and Zn<sub>2</sub>/Al multiatom catalyst. (b) The magnitude of  $k_2$ -weighted Fourier transforms of Zn k-edge EXAFS spectra of the same compounds. (c) XPS spectra in the Zn 2p region of Zn and Zn<sub>2</sub>/Al catalysts. (d) XPS spectra in the Al 2p region of Zn and Zn<sub>2</sub>/Al catalysts. These data were measured after removal of the solvent by calcination. Spectra before calcination are available in the Supporting Information (Figures S3 and S4).

consistent with each other and offer three separate confirmations of the measured surface hydroxyl group—or anchoring site—density. Importantly, all atomic ratios measured by titration for subsequent cycles, including for metal addition, water addition, and ligand release, were within 2%–5% of the values expected based on the structures depicted in Figure 2a, which grew from an isolated hydroxyl group. Zn and Al ratios measured by titration were further confirmed by ICP and XPS (Figure S2). The cluster structures, as shown in Figure 2a, are realistic only at the end of the synthesis, when the solvent can still coordinate to these clusters. After drying and calcination, the clusters are expected to chemically bridge to the surface.

**Characterization of the Multiatom Clusters.** To further confirm these structures, XANES and EXAFS spectra were collected to compare the zinc's chemical environment in both the Zn and Zn<sub>2</sub>/Al catalysts. References of zinc foil, zinc oxide, and zinc acetate were also collected (Figure 3a, b). The XANES spectra of Zn and Zn<sub>2</sub>/Al have edge energies similar to those of zinc oxide and zinc acetate, confirming the presence of zinc(II) ions, similar to the zinc single-atom catalysts reported in the literature.<sup>57</sup> The EXAFS spectra of these two catalysts are all very similar, and only a minor difference of intensity between the two spectra is observable at 9668 eV. Peak assignments were made with reference to literature values of phase-uncorrected Fourier transforms of single-site zinc supported on silica.<sup>58</sup> In both cases, the first shell peak at 1.5 Å, assigned to the Zn–O bond, is the only significant peak detected. This indicates that the zinc atoms are isolated from

each other, as observed previously in case of the Zn single-atom catalyst.<sup>59</sup> In other words, no zinc oxide phase is observed in the Zn catalyst, and zinc atoms are isolated from each other as was expected given the low surface density of anchoring sites. Even though the Zn<sub>2</sub>/Al catalyst contained twice as many zinc atoms, we observed no signs of aggregation. The lack of a peak attributed to the Zn–O–Zn distance also indicates that on each cluster zinc atoms appear to be spaced apart from each other by more than just a single oxygen bridge (and in all likelihood are separated by an additional aluminum atom as suggested). Fitting of the first Zn–O coordination shell spectrum reveals that the zinc atoms are tetracoordinated (SI Table S1, which is in agreement with previously reported literature results<sup>57</sup> and DFT calculations (SI)). However, the coordination number measured ex situ likely differs from the coordination of zinc during catalysis.<sup>57,59</sup> Considering the low loading of metal in our system, further investigation using techniques such as the pair distribution function were not expected to show any significant differences between the catalysts and thus were not considered.

XPS analysis was performed on Al, Zn, and Zn<sub>2</sub>/Al catalysts, and the binding energies measured are consistent with the oxide nature of each element.<sup>60,61</sup> By comparing the Zn and Zn<sub>2</sub>/Al spectrum in the Zn 2p region, we can observe a small but significant peak shift toward higher binding energies when aluminum is present, indicating a decrease of electronic density on the zinc. In contrast, when Al and Zn<sub>2</sub>/Al are compared, a shift toward the lower binding energies is observed, consistent with electron donation to the aluminum atoms. Therefore, the

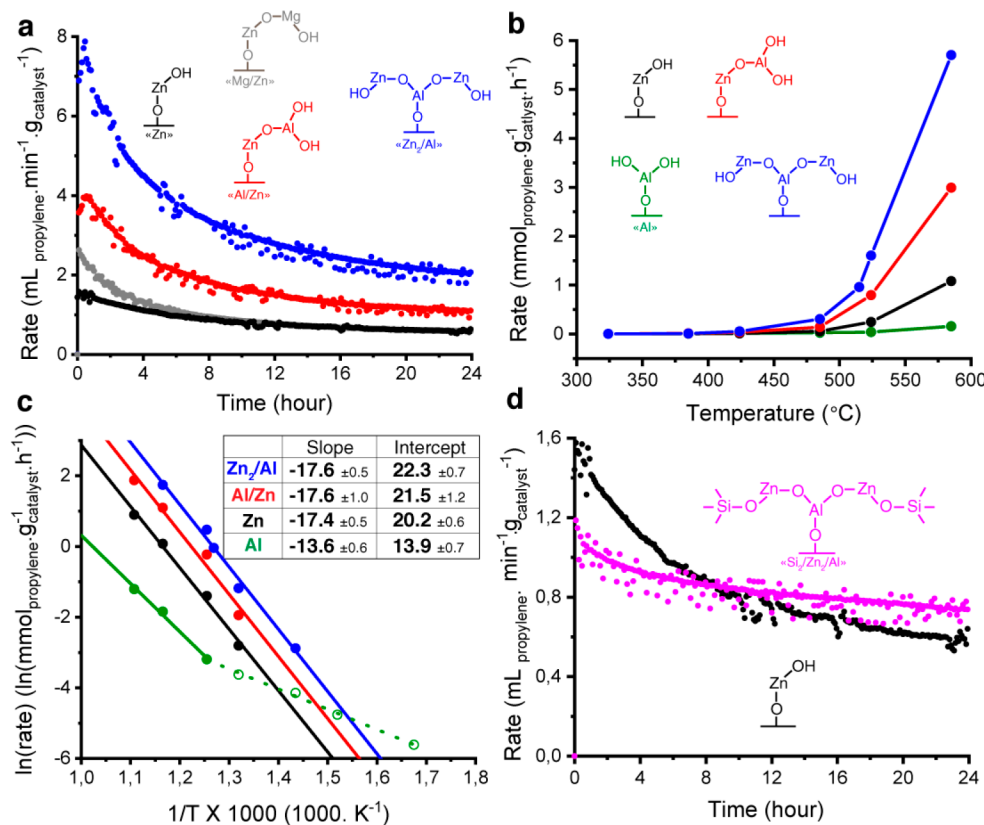


**Figure 4.** (a) Catalytic dehydrogenation of propane to propylene at 550 °C over 24 h in a quartz reactor at conversion below 5%, catalyzed by a Zn single-atom catalyst (black) and Mg/Zn (gray), Al/Zn (red), and Zn<sub>2</sub>/Al (blue) multiatom catalysts. (b) Temperature-programmed reaction of propane dehydrogenation (15% propane in He, 10 °C/min) using Zn and Al single-atom catalysts and Al/Zn and Zn<sub>2</sub>/Al multiatom catalysts. The accuracy of the measurement was checked by repeating the run twice (Figure S12). (c) Arrhenius plots of the Zn and Al single-atom catalysts and Al/Zn and Zn<sub>2</sub>/Al multiatom catalysts. (d) Stability comparison between Zn single-atom catalyst and Si<sub>2</sub>/Zn<sub>2</sub>/Al multiatom catalyst during propane dehydrogenation at 550 °C over 24 h.

aluminum and zinc atoms influence each other's electronic structure, and since inductive effects are known to have a particularly short range, the zinc and aluminum atoms are likely no further away than one bridging oxygen from each other.<sup>62,63</sup>

Solid-state NMR of aluminum was performed on as-prepared and calcined catalysts Al and Zn<sub>2</sub>/Al (Figure S5). In all cases, peaks corresponding to tetraordinated and hexacoordinated aluminum were observed. No peak was attributed to penta-coordinated aluminum, suggesting that no amorphous alumina phase was present, as would have been likely if pure alumina had formed.<sup>45,64</sup> These results are again consistent with the proposed structures and the measured stoichiometric ratio of aluminum:hydroxyl (459 μmol/g Al:439 μmol/g OH). Additionally, 27Al NMR further indicates, by a 2 ppm shift, that a gain of electron density on tetraordinated aluminum has occurred when zinc was present.

Density functional theory (DFT) calculations for different sites, binding modes, and coordination numbers were performed at experimental characterization conditions (i.e., postremoval of the organic solvent). Geometrically, the calculated structures matched experimental observation from XAS and NMR and the electronic effect observed by XPS in our charge calculation (see the most likely structures under experimental conditions and corresponding charges in Figures S6–S8 and Section S2.4).

**Catalytic Tests.** Previous reports have shown that Zn single-atom catalysts can efficiently and selectively convert propane into propylene at 550 °C.<sup>57,58</sup> We used this system as a model reaction to observe possible promotion effects of additional atoms on the reactivity of isolated Zn (Figure 4). Although typical catalyst preparation methods may be simpler, they lead to the formation of a myriad of different active sites, making the structure–activity relationship complicated to establish. The main objective of the synthesis approach presented here is to produce homogeneous well-defined active sites.

The Zn catalyst was used as a reference with an initial propylene production activity of about 1.6 mL propylene min<sup>-1</sup> g catalyst<sup>-1</sup> (Figure 4a). After 24 h, about 40% of the initial activity remained. When a magnesium atom was grafted onto the pendent hydroxyl group of the zinc (catalyst Mg/Zn), a higher initial activity was observed. However, this enhancement did not last long, and the productivity of Mg/Zn ended up falling to the same level as that of Zn after 6 h. When instead of magnesium an aluminum atom was attached to the pendent hydroxyl group of the zinc, the initial activity of Al/Zn was 2.5 times higher than that of the Zn catalyst and remained almost twice as high after 24 h. The final activity was about 28% of its initial value, which indicated a lower intrinsic stability of the catalytic site.

Since aluminum is trivalent, two Zn atoms could react with the pendent hydroxyl groups of one aluminum atom attached

to silica. We tested this structure by measuring the initial activity of  $Zn_2/Al$ , which was approximately twice as high as that of the  $Al/Zn$  catalyst. Therefore, the activity of a zinc site, whether in the form of two zinc atoms grafted to the same aluminum atom or a single zinc atom grafted to a single aluminum atom, appeared to be identically promoted. A comparison on a zinc mass basis further confirms that  $Al/Zn$  and  $Zn_2/Al$  have the same intrinsic activity (Figure S9). After 24 h, the activity of  $Zn_2/Al$  remained twice as high as that of  $Al/Zn$  and about 3.5 times higher than that of the  $Zn$  catalyst alone (about 26% of its own initial activity remained). Our goal was not to create an industrially relevant catalyst, and accordingly, the activity is lower than industrial chromium- and platinum-based catalysts.<sup>65–67</sup> However, the activities were comparable to  $Zn$  catalysts when normalized on a  $Zn$  basis.<sup>57,58</sup> Since our objective was to create homogeneous model catalytic sites with atomic accuracy, we chose a lower zinc surface density to make sure that clusters would not merge during their growth. The catalytic activity of the various materials is reported per mass of catalyst in order to compare their performance as a whole. Since each reactor is loaded with the same amount of catalyst, the quantity of zinc in the reactor when using the  $Zn_2/Al$  catalyst was two times higher than when using  $Zn/Al$ , while the quantity of aluminum is unchanged.

As an additional way to investigate the relationship between the synthesis method and the differences in activity, a control catalyst was prepared with two consecutive cycles of  $Zn$  deposition. After washing and drying, the equivalent of a monolayer of aluminum was added but via a simple incipient wetness impregnation (IWI) of aluminum nitrate hexahydrate. In this case, no promotion in activity was observed (Figure S10). This further demonstrates that the proximity of  $Al$  to  $Zn$  created by the formation of clusters, as opposed to the random structures expected from IWI, is likely responsible for the increase in activity.

To investigate the cause of catalyst deactivation, we performed scanning transmission electron microscopy with high angular dark field (STEM-HAADF) and energy dispersive X-ray (EDX) detectors before and after time on stream of the  $Zn_2/Al$  multiatom catalyst (Figure S11). Elemental mapping before catalysis revealed that both aluminum and zinc were homogeneously dispersed on the silica substrate. Individual zinc or aluminum atoms could not be resolved due to the low contrast between such a light single atom and amorphous silica, even on a high-resolution TEM. However, after catalysis, zinc-rich particles were visible. While the aluminum distribution remained unchanged, zinc migration was observed by the formation of zinc nanoparticles and depletion of zinc in other areas. Moreover, inspection of the quartz reactor after catalysis revealed metallic deposition downstream, which was confirmed to be zinc by ICP and attributed to zinc sublimation (Figure S12). This deposition was observed for all zinc-containing catalysts.

The aforementioned DFT calculations were further used to calculate the adsorption energies of the isolated grafted species (aluminum and zinc as single atoms) and paired species (aluminum and zinc bonded) in our system (Figure S7), which showed that the isolated atoms on the surface were favored compared to their cluster configuration. This result could explain why zinc sites deactivated faster when aluminum is present (Figure 4). Our DFT results show that it is energetically more favorable to have two isolated metals rather

than a cluster with two metal atoms. Dissociation is hence energetically favorable. We hypothesize that the first deactivation reaction was likely to be the separation of zinc from aluminum, which would lead to the loss of the short-range promotion effect observed during catalysis. When such a dissociation from the cluster by a mobile zinc occurs, the occupation of surface sites by  $Al$  could prevent the formation of isolated single sites and further accelerate the agglomeration of mobile zinc that had fewer opportunities to reform single sites, which might explain the increased deactivation and zinc agglomeration when aluminum was present (Figure 4a).

Looking at calculated bond lengths, aluminum always displayed shorter bonds with surface oxygens (1.71–1.73 Å) than zinc (1.85–1.88 Å), highlighting a stronger cation–surface interaction that is consistent with the higher adsorption energy of aluminum than zinc on the surface (Figure S7). This stronger calculated surface interaction helped explain why aluminum remained distributed on the surface while zinc migrated (Figure S11).

Temperature-programmed reactions (TPR) were performed using a ramp of 10 °C/min from 150 to 600 °C to better understand how aluminum influences the onset of zinc activity with temperature (Figure 4b). This technique also facilitated the comparison of initial activity as the temperature ramp was fast enough to prevent any significant deactivation from occurring during the timespan of the experiment (less than 5% of activity loss at the end of the TPR based on the stability study in Figure 4a). Considering the loss of activity for all catalysts on long runs, the structure of some of the active sites are likely changing over time. To approximate the as-made structure as closely as possible, the temperature-programmed reactions were designed to minimize the catalyst's time on stream (30 min). Nevertheless, it is likely that some structural alteration occurred. Consequently, many operating active sites probably differ from the as-prepared structures especially as the reaction progresses. Further (potentially operando) studies would be required to assess the exact effect of these structural changes on the rate. All kinetics measurements used in the Arrhenius plots were performed at conversions lower than 10% to ensure that the measured rates were close to the initial rate (specifically, 7%, 6%, and 3% for  $Al/Zn$ ,  $Zn_2/Al$ , and  $Zn$  catalysts, respectively).

The activity of the reference  $Zn$  single-atom catalyst became detectable between 300 and 350 °C and increased rapidly starting at 425 °C, which is consistent with the literature.<sup>57,68</sup> The maximum rate of production was 1 mmol g<sup>-1</sup> h<sup>-1</sup> with a selectivity of 90%. By comparison, the single-atom catalyst  $Al$  displayed only 15% of  $Zn$  activity at 580 °C and a selectivity on the order of 30%. Some activity was expected as aluminosilicate catalysts are used for alkane dehydrogenation and cracking at the industrial scale.<sup>69–71</sup>  $Al/Zn$ ,  $Zn_2/Al$ , and  $Zn$  displayed an onset of activity at similar temperatures. At the highest temperature, the activity of  $Zn_2/Al$  was twice as high as that of  $Al/Zn$ , which was itself 3 times more active than  $Zn$  while preserving a selectivity of 90%. The enhancement in activity for multiatom catalysts was far larger than the simple addition of each element's own activity measured with single-atom catalysts. These results were consistent with the previous catalytic tests and highlight the promotion of aluminum on zinc activity. The factor of 2 between the measured activities of  $Zn_2/Al$  and  $Al/Zn$  catalysts again strongly suggested that the two zinc atoms of  $Zn_2/Al$ , while grafted on the same aluminum, act as independent catalytic sites. These sites

appeared to be similarly enhanced by the presence of the nearby aluminum atom to what was measured when a single zinc atom was linked to a single aluminum atom. The fact that this ratio of activities is easily explained by the proposed structures (Figure 2a) further supports our conclusion that these structures are indeed correct.

Arrhenius plots were used to compare apparent activation energy and pre-exponential factors of the zinc- and aluminum-containing catalysts (Figure 4c). The Al catalyst seemed to display two regimes (full and empty dots on Figure 4c), but the measured quantities of propylene were near the detection limit of the GC, which complicates interpretation. Comparing slopes, the zinc-containing catalysts appear to all have the same apparent activation energy, which suggests that the rate-limiting step is the same for all zinc-containing catalysts and different from the Al single-atom catalyst. This result also indicates that the zinc atom is the active site even when it has a neighboring aluminum atom. The pre-exponential factor depends on the number of active sites and the entropy of the transition state (the geometrical parameter).<sup>72</sup> The pre-exponential factor of Al/Zn is larger than that of Zn, and since the number of active sites was the same in both cases, this increase can be attributed to a higher entropy of the transition state. At a molecular level, a higher entropy of transition state reflects a greater geometric freedom—or mobility—of the system in the case of Zn/Al compared to Zn only.<sup>72</sup> Comparing Al/Zn and Zn<sub>2</sub>/Al catalysts, the pre-exponential factor increases, which can simply be explained by the previously discussed increased number of active sites present in Zn<sub>2</sub>/Al. From the Arrhenius plots slopes, an apparent activation energy of  $145 \pm 1 \text{ kJ mol}^{-1}$  for all zinc-containing catalysts was calculated, which falls in the expected range from the literature ( $121\text{--}159 \text{ kJ mol}^{-1}$ ).<sup>73,74</sup>

The increased Zn mobility might also favor the displacement of the zinc atom off of the silica surface, leading to irreversible deactivation. Therefore, placing an aluminum next to a zinc atom and adding an anchor on the other side could limit displacement and increase stability. We synthesized a multiatom Si<sub>2</sub>/Zn<sub>2</sub>/Al catalyst by adding Si atoms to better anchor the cluster and compared its propane dehydrogenation activity to the Zn single-atom catalyst (Figure 4d). Initially, the multiatom catalyst has a lower activity, but after 8 h, its increased stability makes it more active on a weight basis. The lower initial activity of Si<sub>2</sub>/Zn<sub>2</sub>/Al compared to the Zn and Zn<sub>2</sub>/Al catalysts was attributed to steric hindrance that limits not only the displacement of Zn but also its accessibility. This behavior illustrates the trade-off between activity and stability of supported atomically dispersed zinc. In contrast, adding a third layer of aluminum did not impact the activity or the stability of the catalyst (Figure S14), suggesting that the presence or absence of promoting an element rather than its quantity is the determining factor. Overall, these results demonstrate that a given atomic configuration can be used to increase activity or stability, but a trade-off appears to exist for this particular system.

## CONCLUSION

We used a stoichiometrically limited liquid-phase atomic layer to grow oxide clusters with different elements atom by atom. We then extensively characterized them and tested their activity for propane dehydrogenation. In doing so, we demonstrated a versatile and atomically precise synthetic method to produce multiatom catalytically active sites. Substantial changes in

activity and stability were obtained by simply varying the elements as well as the order of deposition, where said changes perfectly correlated with the expected structures. Although in this work this method was only applied to a single probe reaction, its modularity could be applied to the design of a wide variety of catalyst clusters for many reactions, potentially leading to the discovery of more active catalysts. Importantly, this procedure can also be used to precisely form uniform multiatomic active sites, as was demonstrated here, which could facilitate the resolution and systematic exploration of atomic promotion effects in catalysis.

## EXPERIMENTAL SECTION

**Support Preparation.** High surface area silica was purchased from Strem Chemicals and dried in a quartz tube at 250 °C (ramp 5 °C/min, then held for 2 h) under vacuum (about  $10^{-2}$  mbar) to remove most of the physisorbed water. The dihydroxylation was driven by ramping the temperature to 800 °C (ramp 2.5 °C/min, hold for 8 h). The silica was then stored in a glovebox (typically <0.1 ppm of H<sub>2</sub>O and <0.1 ppm of O<sub>2</sub>).

**Surface Titration.** A detailed description of the liquid-phase ALD procedure is given in our previous work,<sup>45</sup> but a brief summary is provided below.

We performed a Grignard titration to determine the silica hydroxyl density by adding an excess of methyl magnesium bromide (3 M in ether, Sigma-Aldrich) to a sealed round-bottomed flask containing the prepared silica. The methane released was measured by sampling with a gastight syringe and injected in a PerkinElmer gas chromatography system equipped with a flame ionization detector (GC-FID).

Trimethyl aluminum (Sigma-Aldrich, TMA 2 M in heptane) and diethyl zinc (Acros organics, DEZ 1.5 M in toluene) titrations were performed as follows. In the glovebox, solutions of the target concentration were prepared by diluting commercial solutions with anhydrous dibutyl ether (purchased at Sigma-Aldrich and dried over sodium/benzophenone) using a volumetric flask. The solution was transferred into a sealed Schlenk tube. The silica (typically 2 g) was loaded into a round-bottomed flask with 20 mL of dibutyl ether and capped with a rubber septum.

The water solution was prepared using deionized water that was degassed for 1 h by bubbling nitrogen through the solution. Typically, 0.5 mL of water was added to a Schlenk tube containing 40 mL of anhydrous dioxane (purchased from Sigma-Aldrich and dried with sodium/benzophenone).

All the glassware was transferred from the glovebox to a fume hood where the round-bottomed flask was held on a stirring plate (300 rpm) and the Schlenk tubes connected to a Schlenk line. A small volume of precursor solution was added to the round-bottomed flask every 40 min, and a gas sample was taken before the subsequent injection for analysis by GC-FID to determine the methane released.

Before full coverage, a linear increase of alkane (methane or ethane depending of the precursor involved) released per added reactant was observed (or one mol alkane per mol of precursor). After equivalence, a second slope (about 0.1 methane or ethane per precursor) was observed due to the vapor pressure of the reactant. The crossing point of these two lines gives the equivalence point (i.e., the stoichiometric precursor quantity needed to saturate the hydroxyls on the surface).

**Catalyst Preparation.** The setup for catalyst preparation was the same as for the titration. A round-bottomed flask containing the dispersed support and Schlenk tubes containing precursor solutions were prepared and connected. Every 40 min alternating stoichiometric quantities of precursor and counter-reactant were added from the Schlenk tubes to the round-bottomed flask. The deposition sequence is summarized in Figure 2a. After completion, the catalyst was collected by adding 5 mL of DI water and separated by centrifugation (3000 rpm, 3 min). The powders were washed twice with absolute ethanol to remove any dibutyl ether and dried overnight at 120 °C in a ventilated oven. Remaining traces of organic compounds were removed during the in situ calcination (Figure S14). The silicon

grafting differed in that it was catalyzed by pyridine and stirred overnight. A stoichiometric amount of silicon was added based on pendant hydroxyl groups. The product was then collected in the same way as the other catalysts. More details about the precursors are available in Section S2 of the [Supporting Information](#).

**Catalytic Tests.** The catalytic tests using a quartz reactor were performed using an Autochem II chemisorption setup (Micromeritics). Typically, 100 mg of catalyst was diluted in 0.5 g of silicon carbide (purchased from Strem Chemicals, 100 mesh) to avoid bed clogging and overpressure. The catalyst was calcined in situ (using a 10 °C/min ramp up to 550 °C, at which the reactor was then held for 30 min). Then, the air was purged out with He (30 min, 50 mL/min), and the sample was reduced under hydrogen (30 min, 10% H<sub>2</sub>/90% Ar, 50 mL/min) and purged again with He (30 min, 50 mL/min). The feed was then changed to the reaction mixture at a total flow of 50 mL/min of 30% propane in He for 24 h.

The reaction was monitored using an Agilent GC-FID connected to the outlet of the Autochem, injecting every 5 min. The data processing of the chromatograms was done using MATLAB. Simpson's rule<sup>75</sup> was used to numerically integrate each peak over about 200 points.

A temperature-programmed reaction (TPR) was performed using the same chemisorption apparatus as that used for the catalytic tests. The sampling was performed using a gastight syringe every 5 min. The separation and quantification were performed using a Perkin GC-FID. About 0.3 g of catalyst was used per run. The reaction program consisted of calcination at 300 °C followed by a purge and activation under a hydrogen atmosphere at 300 °C. After these thermal treatments, the temperature was decreased to 250 °C, and the flow of propane was started and given time to stabilize for 30 min. Then, the temperature was ramped up at 10 °C/min from 250 to 600 °C with a constant flow of diluted propane (15% in He, 70 mL/min total).

**Characterization.** Transmission electron microscopy (TEM) was performed using a Talos (FEI) transmission electron microscope working at a 200 keV acceleration voltage. Samples were loaded on Lacey carbon grids by dry mixing.

Diffuse reflectance infrared Fourier transformed spectroscopy (DRIFTS) was performed using a PerkinElmer IR with a sealed sample holder with KBr windows. The samples were loaded into the cell within the glovebox for moisture-sensitive samples. The cell was then sealed and taken out of the glovebox to be mounted on the spectrometer.

X-ray photoelectron spectroscopy (XPS) measurements were carried out on an Axis Supra spectrometer (Kratos Analytical) using the monochromated K $\alpha$  X-ray line of an aluminum anode. The pass energy was set to 40 eV with a step size of 0.2 eV. The samples were electrically insulated from the sample holder, and charges were compensated. Spectra were referenced at 103.5 eV using the SiO<sub>2</sub> bound of the Si 2p transition.

Inductively coupled plasma atomic emission spectroscopy (ICP-AES) was used to quantify metal loading and relative metal ratios in the bimetallic clusters. The samples were first solubilized in concentrated nitric acid overnight to leach out grafted Al and Zn. The solution was filtered to remove particles of silica and analyzed without further treatment.

Magic angle spinning nuclear magnetic resonance (NMR) measurements were performed on a Bruker Neo spectrometer at 21.1 T and a Bruker Advance III spectrometer at 11.7 T. Measurements at 21.1 T were done using a 3.2 mm cross-polarization magic angle spinning (CPMAS) probe at a spin rate of 12.5 kHz. Measurements at 11.7 T were done using a 1.3 mm CPMAS probe at a spin rate of 55 kHz for <sup>27</sup>Al direct measurements with <sup>27</sup>Al  $\pi/2 = 1.8 \mu$ s. All spectra were externally referenced to a 1 M solution of Al(NO<sub>3</sub>)<sub>3</sub> (aq). All <sup>27</sup>Al CP spectra were zero-filled to 8k points and apodized using a Gaussian filter of 1 ms. Spectra were processed using the signal processing program "RMN program".<sup>76</sup>

Zn K-edge X-ray absorption spectroscopy (XAS) experiments were performed at the SuperXAS beamline at the Swiss Light Source (SLS, Paul Scherrer Institute, Switzerland). The beam energy was controlled with a Si(111) quick-EXAFS monochromator.<sup>77</sup> Dried as-synthesized

samples were pressed into pellets, and data were collected in transmission mode using gridded ionization chambers designed for quick data collection. Spectra were collected for 10 min and averaged. Zinc oxide (Sigma-Aldrich) and zinc acetate (Sigma-Aldrich) spectra were collected as references. Samples were calibrated against a zinc metal foil with a known edge energy of 9659 eV. Data fitting was carried out using the Demeter software package.<sup>78</sup>

**Density Functional Theory Calculations.** All density functional theory (DFT) calculations were performed using the pw.x code of Quantum ESPRESSO (v.6.2).<sup>79</sup> The generalized gradient approximation (GGA) to DFT in the Perdew–Burke–Ernzerhof (PBE) formulation was used to optimize the lattice parameters and atomic configuration of all structures.<sup>80</sup> Ultrasoft pseudopotentials were used to describe the interaction between the core and the (semi)valence electrons for all of the atoms. The Kohn–Sham orbitals and total electronic density were expanded in a plane wave basis with 50 and 330 Ry energy cutoffs, respectively.

The silica model structure was taken from Ugliengo et al.<sup>81,82</sup> For all systems, we used a periodic supercell with more than 20 Å of vacuum region in the z direction in order to separate the periodic images. The surface model (containing 204 atoms) was based on a (100) surface. The optimized cell parameters corresponded to an orthorhombic box of 32.00 Å × 16.34 Å × 18.23 Å for SiO<sub>2</sub>.

Adsorption energies have been calculated as

$$E_{\text{Adsorption}} = (E_{\text{Catalyst}} + E_{\text{Water released}}) - (E_{\text{Silica}} - E_{\text{Molecular precursor}})$$

where  $E_{\text{Adsorption}}$  is the adsorption energy,  $E_{\text{Catalyst}}$  the energy of the final material (after grafting),  $E_{\text{Water released}}$  the energy of a water molecule generated by the grafting reaction (condensation of hydroxyl groups),  $E_{\text{Silica}}$  the energy of the silica before grafting, and  $E_{\text{Molecular precursor}}$  the energy of the free molecular precursor, isolated.

## ■ ASSOCIATED CONTENT

### SI Supporting Information

The Supporting Information is available free of charge at <https://pubs.acs.org/doi/10.1021/acssuschemeng.1c07056>.

Additional details on the synthesis, characterization, and catalysis ([PDF](#))

## ■ AUTHOR INFORMATION

### Corresponding Author

Jeremy S. Luterbacher – Laboratory of Sustainable and Catalytic Processes, École Polytechnique Fédérale de Lausanne, 1015 Lausanne, Switzerland; [orcid.org/0000-0002-0967-0583](https://orcid.org/0000-0002-0967-0583); Email: [jeremy.luterbacher@epfl.ch](mailto:jeremy.luterbacher@epfl.ch)

### Authors

Benjamin P. Le Monnier – Laboratory of Sustainable and Catalytic Processes, École Polytechnique Fédérale de Lausanne, 1015 Lausanne, Switzerland

Louisa Savereide – Laboratory of Sustainable and Catalytic Processes, École Polytechnique Fédérale de Lausanne, 1015 Lausanne, Switzerland

Murat Kılıç – Laboratory of Computational Chemistry and Biochemistry, École Polytechnique Fédérale de Lausanne, 1015 Lausanne, Switzerland; [orcid.org/0000-0002-1249-0460](https://orcid.org/0000-0002-1249-0460)

Raphael Schnyder – Laboratory of Sustainable and Catalytic Processes, École Polytechnique Fédérale de Lausanne, 1015 Lausanne, Switzerland

Mounir D. Mensi – Institute of Chemical Science and Engineering, École Polytechnique Fédérale de Lausanne, 1015 Lausanne, Switzerland

Claudia E. Avalos – Institute of Chemical Science and Engineering, École Polytechnique Fédérale de Lausanne, 1015 Lausanne, Switzerland

Ursula Rothlisberger – Laboratory of Computational Chemistry and Biochemistry, École Polytechnique Fédérale de Lausanne, 1015 Lausanne, Switzerland; [orcid.org/0000-0002-1704-8591](https://orcid.org/0000-0002-1704-8591)

Complete contact information is available at:

<https://pubs.acs.org/10.1021/acssuschemeng.1c07056>

### Author Contributions

B.P.L.M. and J.S.L. conceived of the project. B.P.L.M. designed and performed the syntheses, catalytic tests, microscopy characterizations, and infrared analysis. L.S. participated in the data processing of the catalytic tests and fitting of X-ray data. M.K. performed the DFT calculations and visualizations, guided by U.R. who interpreted the DFT results. R.S. participated in the optimization of the synthesis and catalytic tests. M.D.M. performed the XPS measurements. C.E.A. optimized and performed the NMR measurements. J.S.L. and U.R. acquired the funds. All coauthors participated in the writing and editing of the manuscript.

### Notes

The authors declare no competing financial interest.

### ACKNOWLEDGMENTS

This work was supported by the European Research Council (ERC) under the European Union's Horizon 2020 research and innovation program (Starting Grant: CATACOAT, No. 758653) and by EPFL. This work was also accomplished within the framework of the Swiss Competence Center for Bioenergy Research (SCCER-BIOSWEET). The authors wish to acknowledge Dr. Adam Clark and Prof. Maarten Nachtegaal for the access to and acquisition of X-ray absorption spectra at the Swiss Light Source of the Paul Scherrer Institute. We also thank Nathalia Gasilova and Sylvain Coudret for the ICP measurements. Murat Kılıç and Ursula Rothlisberger acknowledge HPC resources of CSCS (Swiss National Supercomputer Centre).

### REFERENCES

- (1) Roldan Cuenya, B.; Beharfarid, F. Nanocatalysis: Size- and Shape-Dependent Chemisorption and Catalytic Reactivity. *Surf. Sci. Rep.* **2015**, *70* (2), 135–187.
- (2) Cargnello, M.; Doan-Nguyen, V. V. T.; Gordon, T. R.; Diaz, R. E.; Stach, E. A.; Gorte, R. J.; Fornasiero, P.; Murray, C. B. Control of Metal Nanocrystal Size Reveals Metal-Support Interface Role for Ceria Catalysts. *Science* **2013**, *341* (6147), 771–773.
- (3) Arzumanov, S. S.; Gabrienko, A. A.; Toktarev, A. V.; Lashchinskaya, Z. N.; Freude, D.; Haase, J.; Stepanov, A. G. Propane Transformation on Zn-Modified Zeolite. Effect of the Nature of Zn Species on Alkane Aromatization and Hydrogenolysis. *J. Phys. Chem. C* **2019**, *123* (50), 30473–30485.
- (4) Kaiser, S. K.; Chen, Z.; Faust Akl, D.; Mitchell, S.; Pérez-Ramírez, J. Single-Atom Catalysts across the Periodic Table. *Chem. Rev.* **2020**, *120* (21), 11703–11809.
- (5) Gawande, M. B.; Fornasiero, P.; Zbořil, R. Carbon-Based Single-Atom Catalysts for Advanced Applications. *ACS Catal.* **2020**, *10* (3), 2231–2259.
- (6) Zhang, H.; Liu, G.; Shi, L.; Ye, J. Single-Atom Catalysts: Emerging Multifunctional Materials in Heterogeneous Catalysis. *Adv. Energy Mater.* **2018**, *8* (1), 1701343.
- (7) Beniya, A.; Higashi, S. Towards Dense Single-Atom Catalysts for Future Automotive Applications. *Nat. Catal.* **2019**, *2* (7), 590–602.

(8) Li, X.; Yang, X.; Huang, Y.; Zhang, T.; Liu, B. Supported Noble-Metal Single Atoms for Heterogeneous Catalysis. *Adv. Mater.* **2019**, *31* (50), 1902031.

(9) Copéret, C.; Comas-Vives, A.; Conley, M. P.; Estes, D. P.; Fedorov, A.; Mougél, V.; Nagae, H.; Núñez-Zarur, F.; Zhizhko, P. A. Surface Organometallic and Coordination Chemistry toward Single-Site Heterogeneous Catalysts: Strategies, Methods, Structures, and Activities. *Chem. Rev.* **2016**, *116* (2), 323–421.

(10) Samantaray, M. K.; Pump, E.; Bendjeriou-Sedjerari, A.; D'Elia, V.; Pelletier, J. D. A.; Guidotti, M.; Psaro, R.; Basset, J.-M. Surface Organometallic Chemistry in Heterogeneous Catalysis. *Chem. Soc. Rev.* **2018**, *47* (22), 8403–8437.

(11) Lee, J.-K.; Kung, M. C.; Kung, H. H. Cooperative Catalysis: A New Development in Heterogeneous Catalysis. *Top. Catal.* **2008**, *49* (3), 136–144.

(12) Peng, W.; Feng, Y.; Yan, X.; Hou, F.; Wang, L.; Liang, J. Multiatom Catalysts for Energy-Related Electrocatalysis. *Adv. Sustain. Syst.* **2021**, *5*, 2000213.

(13) Guan, E.; Ciston, J.; Bare, S. R.; Runnebaum, R. C.; Katz, A.; Kulkarni, A.; Kronawitter, C. X.; Gates, B. C. Supported Metal Pair-Site Catalysts. *ACS Catal.* **2020**, *10* (16), 9065–9085.

(14) Hayek, K.; Kramer, R.; Paál, Z. Metal-Support Boundary Sites in Catalysis. *Appl. Catal. Gen.* **1997**, *162* (1), 1–15.

(15) Kaneda, K.; Mitsudome, T. Metal-Support Cooperative Catalysts for Environmentally Benign Molecular Transformations. *Chem. Rev.* **2017**, *17* (1), 4–26.

(16) Novaro, O.; Chow, S.; Magnouat, P. Mechanism of Oligomerization of Alpha Olefins with Ziegler-Natta Catalysts. *J. Catal.* **1976**, *41*, 91–100.

(17) Wang, L.; Guan, E.; Zhang, J.; Yang, J.; Zhu, Y.; Han, Y.; Yang, M.; Cen, C.; Fu, G.; Gates, B. C.; Xiao, F.-S. Single-Site Catalyst Promoters Accelerate Metal-Catalyzed Nitroarene Hydrogenation. *Nat. Commun.* **2018**, *9* (1), 1–8.

(18) Paterson, J.; Potter, M.; Gianotti, E.; Raja, R. Engineering Active Sites for Enhancing Synergy in Heterogeneous Catalytic Oxidations. *Chem. Commun.* **2011**, *47* (1), 517–519.

(19) Jiao, J.; Lin, R.; Liu, S.; Cheong, W.-C.; Zhang, C.; Chen, Z.; Pan, Y.; Tang, J.; Wu, K.; Hung, S.-F.; Chen, H. M.; Zheng, L.; Lu, Q.; Yang, X.; Xu, B.; Xiao, H.; Li, J.; Wang, D.; Peng, Q.; Chen, C.; Li, Y. Copper Atom-Pair Catalyst Anchored on Alloy Nanowires for Selective and Efficient Electrochemical Reduction of CO<sub>2</sub>. *Nat. Chem.* **2019**, *11* (3), 222–228.

(20) Bakandritsos, A.; Kadam, R. G.; Kumar, P.; Zoppellaro, G.; Medved', M.; Tuček, J.; Montini, T.; Tomanec, O.; Andrášková, P.; Drahoš, B.; Varma, R. S.; Otyepka, M.; Gawande, M. B.; Fornasiero, P.; Zbořil, R. Mixed-Valence Single-Atom Catalyst Derived from Functionalized Graphene. *Adv. Mater.* **2019**, *31* (17), 1900323.

(21) Desai, S. P.; Ye, J.; Zheng, J.; Ferrandon, M. S.; Webber, T. E.; Platero-Prats, A. E.; Duan, J.; Garcia-Holley, P.; Camaioni, D. M.; Chapman, K. W.; Delferro, M.; Farha, O. K.; Fulton, J. L.; Gagliardi, L.; Lercher, J. A.; Penn, R. L.; Stein, A.; Lu, C. C. Well-Defined Rhodium–Gallium Catalytic Sites in a Metal–Organic Framework: Promoter-Controlled Selectivity in Alkyne Semihydrogenation to E-Alkenes. *J. Am. Chem. Soc.* **2018**, *140* (45), 15309–15318.

(22) Calle-Vallejo, F.; Tymoczko, J.; Colic, V.; Vu, Q. H.; Pohl, M. D.; Morgenstern, K.; Löffreda, D.; Sautet, P.; Schuhmann, W.; Bandarenka, A. S. Finding Optimal Surface Sites on Heterogeneous Catalysts by Counting Nearest Neighbors. *Science* **2015**, *350* (6257), 185–189.

(23) George, S. M. Atomic Layer Deposition: An Overview. *Chem. Rev.* **2010**, *110* (1), 111–131.

(24) Leskelä, M.; Ritala, M. Atomic Layer Deposition Chemistry: Recent Developments and Future Challenges. *Angew. Chem., Int. Ed.* **2003**, *42* (45), 5548–5554.

(25) Lu, J.; Elam, J. W.; Stair, P. C. Atomic Layer Deposition—Sequential Self-Limiting Surface Reactions for Advanced Catalyst “Bottom-up” Synthesis. *Surf. Sci. Rep.* **2016**, *71* (2), 410–472.

(26) Lu, J.; Fu, B.; Kung, M. C.; Xiao, G.; Elam, J. W.; Kung, H. H.; Stair, P. C. Coking- and Sintering-Resistant Palladium Catalysts

- Achieved Through Atomic Layer Deposition. *Science* **2012**, *335* (6073), 1205–1208.
- (27) Pagán-Torres, Y. J.; Gallo, J. M. R.; Wang, D.; Pham, H. N.; Libera, J. A.; Marshall, C. L.; Elam, J. W.; Datsy, A. K.; Dumesic, J. A. Synthesis of Highly Ordered Hydrothermally Stable Mesoporous Niobia Catalysts by Atomic Layer Deposition. *ACS Catal.* **2011**, *1* (10), 1234–1245.
- (28) O'Neill, B. J.; Jackson, D. H. K.; Crisci, A. J.; Farberow, C. A.; Shi, F.; Alba-Rubio, A. C.; Lu, J.; Dietrich, P. J.; Gu, X.; Marshall, C. L.; Stair, P. C.; Elam, J. W.; Miller, J. T.; Ribeiro, F. H.; Voyles, P. M.; Greeley, J.; Mavrikakis, M.; Scott, S. L.; Kuech, T. F.; Dumesic, J. A. Stabilization of Copper Catalysts for Liquid-Phase Reactions by Atomic Layer Deposition. *Angew. Chem.* **2013**, *125* (51), 14053–14057.
- (29) Feng, H.; Libera, J. A.; Stair, P. C.; Miller, J. T.; Elam, J. W. Subnanometer Palladium Particles Synthesized by Atomic Layer Deposition. *ACS Catal.* **2011**, *1* (6), 665–673.
- (30) Li, J.; Liang, X.; King, D. M.; Jiang, Y.-B.; Weimer, A. W. Highly Dispersed Pt Nanoparticle Catalyst Prepared by Atomic Layer Deposition. *Appl. Catal. B Environ.* **2010**, *97* (1–2), 220–226.
- (31) Gould, T. D.; Lubers, A. M.; Neltner, B. T.; Carrier, J. V.; Weimer, A. W.; Falconer, J. L.; Will Medlin, J. Synthesis of Supported Ni Catalysts by Atomic Layer Deposition. *J. Catal.* **2013**, *303*, 9–15.
- (32) Cheng, N.; Sun, X. Single Atom Catalyst by Atomic Layer Deposition Technique. *Chin. J. Catal.* **2017**, *38* (9), 1508–1514.
- (33) Piernavieja-Hermida, M.; Lu, Z.; White, A.; Low, K.-B.; Wu, T.; Elam, J. W.; Wu, Z.; Lei, Y. Towards ALD Thin Film Stabilized Single-Atom Pd 1 Catalysts. *Nanoscale* **2016**, *8* (33), 15348–15356.
- (34) Christensen, S. T.; Feng, H.; Libera, J. L.; Guo, N.; Miller, J. T.; Stair, P. C.; Elam, J. W. Supported Ru–Pt Bimetallic Nanoparticle Catalysts Prepared by Atomic Layer Deposition. *Nano Lett.* **2010**, *10* (8), 3047–3051.
- (35) Zhang, L.; Si, R.; Liu, H.; Chen, N.; Wang, Q.; Adair, K.; Wang, Z.; Chen, J.; Song, Z.; Li, J.; Banis, M. N.; Li, R.; Sham, T.-K.; Gu, M.; Liu, L.-M.; Botton, G. A.; Sun, X. Atomic Layer Deposited Pt–Ru Dual-Metal Dimers and Identifying Their Active Sites for Hydrogen Evolution Reaction. *Nat. Commun.* **2019**, *10* (1), 4936.
- (36) Yan, H.; Lin, Y.; Wu, H.; Zhang, W.; Sun, Z.; Cheng, H.; Liu, W.; Wang, C.; Li, J.; Huang, X.; Yao, T.; Yang, J.; Wei, S.; Lu, J. Bottom-up Precise Synthesis of Stable Platinum Dimers on Graphene. *Nat. Commun.* **2017**, *8* (1), 1070.
- (37) Puurunen, R. L.; Vandervorst, W. Island Growth as a Growth Mode in Atomic Layer Deposition: A Phenomenological Model. *J. Appl. Phys.* **2004**, *96* (12), 7686–7695.
- (38) Hagen, D. J.; Connolly, J.; Povey, I. M.; Rushworth, S.; Pemble, M. E. Island Coalescence during Film Growth: An Underestimated Limitation of Cu ALD. *Adv. Mater. Interfaces* **2017**, *4* (18), 1700274.
- (39) Terranova, U.; Bowler, D. R. Effect of Hydration of the TiO<sub>2</sub> Anatase (101) Substrate on the Atomic Layer Deposition of Alumina Films. *J. Mater. Chem.* **2011**, *21* (12), 4197.
- (40) Wilson, C. A.; Grubbs, R. K.; George, S. M. Nucleation and Growth during Al<sub>2</sub>O<sub>3</sub> Atomic Layer Deposition on Polymers. *Chem. Mater.* **2005**, *17* (23), S625–S634.
- (41) Elam, J. W.; Zinovev, A. V. V.; Pellin, M. J.; Comstock, D. J.; Hersam, M. C. Nucleation and Growth of Noble Metals on Oxide Surfaces Using Atomic Layer Deposition. *ECS Transactions* **2007**, *3*, 271–278.
- (42) Elam, J. W.; Nelson, C. E.; Grubbs, R. K.; George, S. M. Nucleation and Growth during Tungsten Atomic Layer Deposition on SiO<sub>2</sub> Surfaces. *Thin Solid Films* **2001**, *386* (1), 41–52.
- (43) Dendooven, J.; Van Daele, M.; Solano, E.; Ramachandran, R. K.; Minjauw, M. M.; Resta, A.; Vlad, A.; Garreau, Y.; Coati, A.; Portale, G.; Detavernier, C. Surface Mobility and Impact of Precursor Dosing during Atomic Layer Deposition of Platinum: *In Situ* Monitoring of Nucleation and Island Growth. *Phys. Chem. Chem. Phys.* **2020**, *22*, 24917.
- (44) White, R. L.; Nair, A. Diffuse Reflectance Infrared Spectroscopic Characterization of Silica Dehydroxylation. *Appl. Spectrosc.* **1990**, *44* (1), 69–75.
- (45) Le Monnier, B. P.; Wells, F.; Talebkeikhah, F.; Luterbacher, J. S. Atomic Layer Deposition on Dispersed Materials in Liquid Phase by Stoichiometrically Limited Injections. *Adv. Mater.* **2019**, *31* (52), 1904276.
- (46) Li, J.; DiVerdi, J. A.; Maciel, G. E. Chemistry of the Silica Surface: Liquid–Solid Reactions of Silica Gel with Trimethylaluminum. *J. Am. Chem. Soc.* **2006**, *128* (51), 17093–17101.
- (47) Kermagoret, A.; Kerber, R. N.; Conley, M. P.; Callens, E.; Florian, P.; Massiot, D.; Coperet, C.; Delbecq, F.; Rozanska, X.; Sautet, P. Triisobutylaluminum: Bulkier and yet More Reactive towards Silica Surfaces than Triethyl or Trimethylaluminum. *Dalton Trans.* **2013**, *42* (35), 12681–12687.
- (48) Park, D.-H.; Nishiyama, N.; Egashira, Y.; Ueyama, K. Enhancement of Hydrothermal Stability and Hydrophobicity of a Silica MCM-48 Membrane by Silylation. *Ind. Eng. Chem. Res.* **2001**, *40* (26), 6105–6110.
- (49) Mole, T.; Jeffery, E. A. Trialkylaluminiums. In *Organometallic Compounds*; Elsevier, 1972; pp 85–128.
- (50) Dugas, V.; Chevalier, Y. Surface Hydroxylation and Silane Grafting on Fumed and Thermal Silica. *J. Colloid Interface Sci.* **2003**, *264* (2), 354–361.
- (51) Rubio, J.; Kitchener, J. A. The Mechanism of Adsorption of Poly(Ethylene Oxide) Flocculant on Silica. *J. Colloid Interface Sci.* **1976**, *57* (1), 132–142.
- (52) Zhuravlev, L. T. The Surface Chemistry of Amorphous Silica. Zhuravlev Model. *Colloids Surf. Physicochem. Eng. Asp.* **2000**, *173* (1), 1–38.
- (53) Morrow, B. A.; Cody, I. A. Infrared Studies of Reactions on Oxide Surfaces. 5. Lewis Acid Sites on Dehydroxylated Silica. *J. Phys. Chem.* **1976**, *80* (18), 1995–1998.
- (54) Werghi, B.; Bendjeriou-Sedjerari, A.; Jedidi, A.; Abou-Hamad, E.; Cavallo, L.; Basset, J.-M. Single-Site Tetracoordinated Aluminum Hydride Supported on Mesoporous Silica. From Dream to Reality! *Organometallics* **2016**, *35* (19), 3288–3294.
- (55) Duchateau, R.; van Meerendonk, W. J.; Huijser, S.; Staal, B. B. P.; van Schilt, M. A.; Gerritsen, G.; Meetsma, A.; Koning, C. E.; Kemmere, M. F.; Keurentjes, J. T. F. Silica-Grafted Diethylzinc and a Silsesquioxane-Based Zinc Alkyl Complex as Catalysts for the Alternating Oxirane–Carbon Dioxide Copolymerization. *Organometallics* **2007**, *26* (17), 4204–4211.
- (56) Camacho-Bunquin, J.; Ferrandon, M.; Das, U.; Dogan, F.; Liu, C.; Larsen, C.; Platero-Prats, A. E.; Curtiss, L. A.; Hock, A. S.; Miller, J. T.; Nguyen, S. T.; Marshall, C. L.; Delferro, M.; Stair, P. C. Supported Aluminum Catalysts for Olefin Hydrogenation. *ACS Catal.* **2017**, *7* (1), 689–694.
- (57) Schweitzer, N. M.; Hu, B.; Das, U.; Kim, H.; Greeley, J.; Curtiss, L. A.; Stair, P. C.; Miller, J. T.; Hock, A. S. Propylene Hydrogenation and Propane Dehydrogenation by a Single-Site Zn<sup>2+</sup> on Silica Catalyst. *ACS Catal.* **2014**, *4* (4), 1091–1098.
- (58) Camacho-Bunquin, J.; Aich, P.; Ferrandon, M.; Getsoian, A.; Das, U.; Dogan, F.; Curtiss, L. A.; Miller, J. T.; Marshall, C. L.; Hock, A. S.; Stair, P. C. Single-Site Zinc on Silica Catalysts for Propylene Hydrogenation and Propane Dehydrogenation: Synthesis and Reactivity Evaluation Using an Integrated Atomic Layer Deposition-Catalysis Instrument. *J. Catal.* **2017**, *345*, 170–182.
- (59) Das, U.; Zhang, G.; Hu, B.; Hock, A. S.; Redfern, P. C.; Miller, J. T.; Curtiss, L. A. Effect of Siloxane Ring Strain and Cation Charge Density on the Formation of Coordinately Unsaturated Metal Sites on Silica: Insights from Density Functional Theory (DFT) Studies. *ACS Catal.* **2015**, *5* (12), 7177–7185.
- (60) Rotole, J. A.; Sherwood, P. M. A. Boehmite ( $\gamma$ -AlOOH) by XPS. *Surf. Sci. Spectra* **1998**, *5* (1), 53–59.
- (61) Biesinger, M. C.; Lau, L. W. M.; Gerson, A. R.; Smart, R. St. C. Resolving Surface Chemical States in XPS Analysis of First Row Transition Metals, Oxides and Hydroxides: Sc, Ti, V, Cu and Zn. *Appl. Surf. Sci.* **2010**, *257* (3), 887–898.
- (62) Marshall, S. T.; Medlin, J. W. Surface-Level Mechanistic Studies of Adsorbate–Adsorbate Interactions in Heterogeneous Catalysis by Metals. *Surf. Sci. Rep.* **2011**, *66* (5), 173–184.

- (63) Kuznetsov, D. A.; Han, B.; Yu, Y.; Rao, R. R.; Hwang, J.; Román-Leshkov, Y.; Shao-Horn, Y. Tuning Redox Transitions via Inductive Effect in Metal Oxides and Complexes, and Implications in Oxygen Electrocatalysis. *Joule* **2018**, *2* (2), 225–244.
- (64) Baca, M.; de la Rochefoucauld, E.; Ambrose, E.; Krafft, J.-M.; Hajjar, R.; Man, P. P.; Carrier, X.; Blanchard, J. Characterization of Mesoporous Alumina Prepared by Surface Alumination of SBA-15. *Microporous Mesoporous Mater.* **2008**, *110* (2–3), 232–241.
- (65) Wang, G.; Zhu, X.; Li, C. Recent Progress in Commercial and Novel Catalysts for Catalytic Dehydrogenation of Light Alkanes. *Chem. Rec.* **2020**, *20*, 604.
- (66) Hu, Z.-P.; Yang, D.; Wang, Z.; Yuan, Z.-Y. State-of-the-Art Catalysts for Direct Dehydrogenation of Propane to Propylene. *Chin. J. Catal.* **2019**, *40* (9), 1233–1254.
- (67) de Miguel, S. R.; Jablonski, E. L.; Castro, A. A.; Scelza, O. A Highly Selective and Stable Multimetallic Catalysts for Propane Dehydrogenation. *J. Chem. Technol. Biotechnol.* **2000**, *75* (7), 596–600.
- (68) Kolyagin, Y.; Ordonsky, V.; Khimiyak, Y.; Rebrov, A.; Fajula, F.; Ivanova, I. Initial Stages of Propane Activation over Zn/MFI Catalyst Studied by in Situ NMR and IR Spectroscopic Techniques. *J. Catal.* **2006**, *238* (1), 122–133.
- (69) Brenner, A.; Emmett, P. H. Dehydrogenation—The First Step in the Cracking of Isopentane over Silica-Alumina Cracking Catalysts. *J. Catal.* **1982**, *75* (2), 410–415.
- (70) Ivanov, V. A.; Bachelier, J.; Audry, F.; Lavalley, J. C. Study of the Meerwein—Ponndorf—Verley Reaction between Ethanol and Acetone on Various Metal Oxides. *J. Mol. Catal.* **1994**, *91* (1), 45–59.
- (71) Busca, G. Silica-Alumina Catalytic Materials: A Critical Review. *Catal. Today* **2020**, *357*, 621–629.
- (72) Chorkendorff, I.; Niemantsverdriet, J. W. Reaction Rate Theory. In *Concepts of Modern Catalysis and Kinetics*; John Wiley & Sons, 2006; pp 79–128.
- (73) Nozik, D.; Tinga, F. M. P.; Bell, A. T. Propane Dehydrogenation and Cracking over Zn/H-MFI Prepared by Solid-State Ion Exchange of ZnCl<sub>2</sub>. *ACS Catal.* **2021**, *11*, 14489–14506.
- (74) Wan, B.-Z.; Chu, H. M. Reaction Kinetics of Propane Dehydrogenation over Partially Reduced Zinc Oxide Supported on Silicalite. *J. Chem. Soc. Faraday Trans.* **1992**, *88* (19), 2943–2947.
- (75) Abramowitz, M.; Stegun, I. A. Numerical Interpolation, Differentiation, and integration. In *Handbook of Mathematical Functions with Formulas, Graphs, and Mathematical Tables*; Dover Publications, 1970; pp 877–924.
- (76) Grandinetti, P. J. RMN program. <https://www.physyapps.com/rmn-intuitive-signal-processing-physical-sciences>.
- (77) Müller, O.; Nachtegaal, M.; Just, J.; Lützenkirchen-Hecht, D.; Frahm, R. Quick-EXAFS Setup at the SuperXAS Beamline for in Situ X-Ray Absorption Spectroscopy with 10 Ms Time Resolution. *J. Synchrotron Radiat.* **2016**, *23* (1), 260–266.
- (78) Ravel, B.; Newville, M. ATHENA, ARTEMIS, HEPHAESTUS: Data Analysis for X-Ray Absorption Spectroscopy Using IFEFFIT. *J. Synchrotron Radiat.* **2005**, *12* (4), 537–541.
- (79) Giannozzi, P.; Baroni, S.; Bonini, N.; Calandra, M.; Car, R.; Cavazzoni, C.; Ceresoli, D.; Chiarotti, G. L.; Cococcioni, M.; Dabo, I.; Dal Corso, A.; de Gironcoli, S.; Fabris, S.; Fratesi, G.; Gebauer, R.; Gerstmann, U.; Gougoussis, C.; Kokalj, A.; Lazzeri, M.; Martin-Samos, L.; Marzari, N.; Mauri, F.; Mazzarello, R.; Paolini, S.; Pasquarello, A.; Paulatto, L.; Sbraccia, C.; Scandolo, S.; Sclauzero, G.; Seitonen, A. P.; Smogunov, A.; Umari, P.; Wentzcovitch, R. M. QUANTUM ESPRESSO: A Modular and Open-Source Software Project for Quantum Simulations of Materials. *J. Phys.: Condens. Matter* **2009**, *21* (39), 395502.
- (80) Perdew, J. P.; Burke, K.; Wang, Y. Generalized Gradient Approximation for the Exchange-Correlation Hole of a Many-Electron System. *Phys. Rev. B* **1996**, *54* (23), 16533–16539.
- (81) Ugliengo, P.; Sodupe, M.; Musso, F.; Bush, I. J.; Orlando, R.; Dovisi, R. Realistic Models of Hydroxylated Amorphous Silica Surfaces and MCM-41 Mesoporous Material Simulated by Large-Scale Periodic B3LYP Calculations. *Adv. Mater.* **2008**, *20* (23), 4579–4583.
- (82) Macià Escatllar, A.; Ugliengo, P.; Bromley, S. T. Modeling Hydroxylated Nanosilica: Testing the Performance of ReaxFF and FFSiOH Force Fields. *J. Chem. Phys.* **2017**, *146* (22), 224704.

## Recommended by ACS

### Molybdenum Oxide Clusters: Structure, Stability, and Electronic Properties

Aslihan Sumer.

JUNE 03, 2021  
THE JOURNAL OF PHYSICAL CHEMISTRY A

READ 

### Co–Ru Nanoalloy Catalysts for the Acceptorless Dehydrogenation of Alcohols

Brandon Azeredo, Jean-Yves Piquemal, et al.

MARCH 23, 2022  
ACS APPLIED NANO MATERIALS

READ 

### On the Cobalt Carbide Formation in a Co/TiO<sub>2</sub> Fischer–Tropsch Synthesis Catalyst as Studied by High-Pressure, Long-Term Operando X-ray Absorption an...

Ilse K. van Ravenhorst, Bert M. Weckhuysen, et al.

FEBRUARY 19, 2021  
ACS CATALYSIS

READ 

### Fine-Tuning the Activity of Metal–Organic Framework-Supported Cobalt Catalysts for the Oxidative Dehydrogenation of Propane

Zhanyong Li, Omar K. Farha, et al.

OCTOBER 04, 2017  
JOURNAL OF THE AMERICAN CHEMICAL SOCIETY

READ 

Get More Suggestions >